TECHNICAL PAPER

JOURNAL OF THE SOUTH AFRICAN INSTITUTION OF CIVIL ENGINEERING
ISSN 1021-2019 (print) | ISSN 2309-8775 (online)
Vol 67 No 3, December 2025, Pages 40–53, Paper 1766

The measured and modelled thermal response of reinforced concrete T-beams subjected to environmental loading

A Kleynhans, EP Kearsley, SA Skorpen

In this study, the thermal response of two reinforced concrete T-beams with identical outer dimensions but differing internal geometry, and therefore different thermal inertia, is investigated. Both T-beams were instrumented with thermocouples and vibrating wire strain gauges and subjected to purely thermal environmental loading. The weighted average (effective cross-sectional) temperature, along with the vertical and transverse temperature distributions, were analysed. In addition, theoretical thermal strains and self-equilibrating stresses were calculated. Uniquely, the mathematical model and assumptions were compared to and validated by experimentally measured strains as opposed to validation through comparisons of predicted temperatures. Effective temperature ranges were related to cross-sectional area per unit width and compared to results from literature. Furthermore, the greatest difference in thermal response between the two sections was found to be effective temperature and subsequent longitudinal movement. Calculated bending moments, caused by thermal loading effects and self-equilibrating stresses, approached 30% of the concrete's ultimate tensile capacity, emphasising their structural relevance.

Keywords: reinforced concrete, thermal response, thermal inertia, cross-sectional geometry, environmental loading

AMÉ KLEYNHANS is a PhD candidate in Civil Engineering at the University of Pretoria, where she also obtained her BEng, BEng (Hons) and MEng degrees, all with distinction. Her doctoral research focuses on the interaction between steel and concrete in reinforced elements, with emphasis on time-dependent material behaviour and internal stress development. Building on her master's research into the environmental loading of reinforced concrete, her current work integrates laboratory investigations and monitoring with field-based structural health monitoring data analysis to improve understanding of long-term structural behaviour.

Contact details:
Department of Civil Engineering
University of Pretoria
Hatfield 0028
South Africa
ame.kleynhans@tuks.co.za

PROF ELSABÉ KEARSLEY (Pr Eng, FSAICE, FSAAE) was the 2009 SAICE President and is currently a Professor of Civil Engineering at the University of Pretoria. Her research focusses on reducing the environmental impact of the cement and concrete industry. She has been supervising postgraduate research students and conducts both experimental laboratory studies to determine the effect of different waste streams and mix compositions on concrete properties, as well as structural health monitoring of concrete infrastructure to determine the effect of environmental conditions on concrete behaviour over extended periods of time.

Contact details:
Department of Civil Engineering
University of Pretoria
Hatfield 0028
South Africa
elsabe.kearsley@up.ac.za

DR SARAH SKORPEN (Pr Eng, FSAICE) is a Senior Lecturer in the Department of Civil Engineering at the University of Pretoria. She is involved in structural engineering research and teaches structural design courses at both undergraduate and postgraduate levels. Her current research interests include the structural behaviour of concrete bridges, particularly integral bridges, and structural health monitoring.

Contact details:
Department of Civil Engineering
University of Pretoria
Hatfield 0028
South Africa
sarah.skorpen@up.ac.za

PRACTICAL APPLICATIONS

The study shows the critical influence of cross-sectional geometry and thermal inertia on a structure's response to environmental thermal loading. The findings suggest that strategically increasing thermal inertia – achieved, for example, by employing solid sections instead of box girders – can effectively mitigate thermal movement. This can be beneficial for monolithic construction, such as integral bridges. Examining both transverse and vertical temperature distributions can be used to improve standard design codes and minimise internal stresses through optimised cross-sectional design, increasing the efficiency and longevity of structures to environmental thermal conditions.

INTRODUCTION

Concrete is often used for bridge construction due to its availability, versatility, and durability. However, many designers and researchers have reported concrete cracking, damage, and decreased service life due to environmental thermal loading experienced by concrete bridges (Priestly 1978, Dilger *et al* 1983, Elbadry & Ghali 1986, Branco & Mendes 1993, Moravcik & Krkoska 2017, Hagedorn *et al* 2019, Abid *et al* 2021). There are numerous reports that thermal loading could equal or even exceed the magnitude of design live loads, highlighting the need to consider thermal environmental loading accurately in design (Radolli & Green 1975, Elbadry & Ghali 1986, Vecchio 1987, Gu *et al* 2014, Feng *et al* 2022). The movements of expansion and contraction caused by mean effective deck temperature changes are accommodated by bearings and expansion joints in most bridge typologies. Nonetheless, accurate design movements are required to optimise the selection and design of joints and

A Kleynhans, EP Kearsley, SA Skorpen. The measured and modelled thermal response of reinforced concrete T-beams subjected to environmental loading. J. S. Afr. Inst. Civ. Eng. 2025:67(3), Art. #1766, 14 pages. http://dx.doi.org/10.17159/2309-8775/2025/v67n3a4

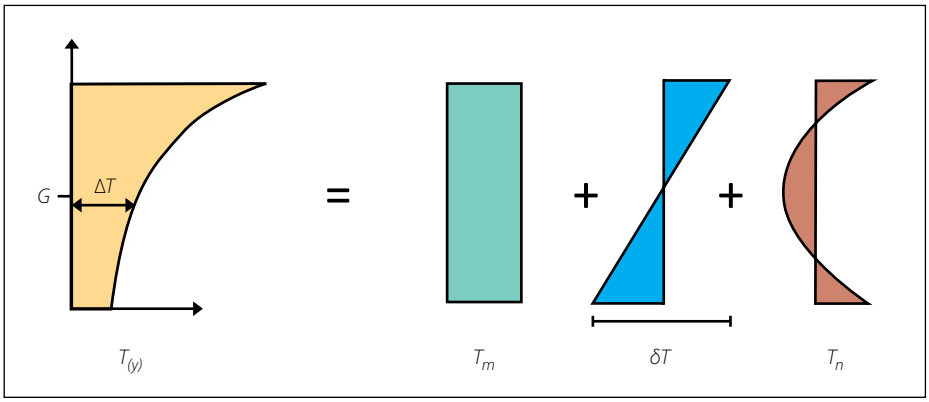

Figure 1 Temperature components (adapted from Branco & Mendes 1993)

bearings, minimising the cost of initial construction and maintenance (Roeder 2003, Peiretti *et al* 2014).

Concrete has poor thermal conductivity, a characteristic that causes large non-linear temperature differentials, particularly through the depth of cross sections with daily temperature cycles (Potgieter 1983, Lee 2012, Abid 2018). Fu *et al* (1990) confirmed that steady-state thermal conditions never exist within bridge structures, since ambient air temperature and solar radiation intensity are both time dependent. According to Branco and Mendes (1993), non-linear temperature distributions can be decomposed into three components, namely a uniform temperature T_m, a linear gradient for each direction with a temperature difference δT and a non-linear distribution T_n (Figure 1).

The first component is associated with longitudinal displacement, but even with the incorporation of bearings and expansion joints, friction can cause partial restraint of longitudinal movements, resulting in significant force and stress development in a cross section (Hoffman *et al* 1983, Moorty & Roeder 1992).

The second component (δT) is associated with curvature. Typically, a 'positive gradient' refers to members which have greater temperatures at the top surface compared to the bottom, and 'negative gradients' for the inverted case. In the absence of restraint, upward hogging results from positive gradients, while negative gradients cause sagging. However, for continuous structures where internal supports prevent curvature, large bending stresses develop in the cross section. The nonlinear temperature component produces self-equilibrating stresses which arise due to the incompatibility between the requirements that plane sections remain plane according to Euler-Bernoulli beam theory, and that individual fibres would expand by an amount proportional to local temperature rise, if not restrained by adjacent fibres (Priestly 1972, Elbadry & Ghali 1986, Vecchio 1987).

The non-linear temperature component is the only component that produces stress regardless of external boundary conditions. While the temperature distributions and gradients referred to in literature primarily focus on the vertical variations along cross-sectional depth, non-linear temperature distributions may also develop across the width, or in the transverse direction, of a section. The thermal response and, by extension, the stress distribution of a bridge deck is dependent on its cross-sectional geometry (Radolli & Green 1975, Imbsen *et al* 1985). Various authors have conducted research on the effects of varying cross-sectional geometric dimensions on temperature distributions. Mirambell and Aguado (1990) concluded that superstructure depth and the ratio between width of the upper and lower slab of box-girders had the greatest influence on the vertical temperature distribution, while web-overhang ratio had the greatest influence on transverse temperature variations. Hagedorn *et al* (2019) studied concrete I-girder decks and concluded that transverse temperature variations can be significant and that noticeable longitudinal curvature occurred because the girders were placed in an east-west orientation, such that one side was always shaded. Gu *et al* (2014) compared the temperature distributions of two cross sections from the same concrete box girder bridge and attributed the differences in temperature distributions to the changes in thicknesses of the web and bottom slab. Analysis of rectangular, T- and I-sections completed by Radolli and Green (1975) concluded that temperature distribution, maximum curvature, and mean temperature depend on section depth and that shallow sections exhibit larger curvature and higher mean temperatures, while deeper sections result in lower curvature and high self-equilibrating stresses. Branco and Mendes (1993) also found that depth influences the temperature gradients of concrete T-beams, slabs and box-girders.

All these thermal deck studies are related to the concept of thermal inertia. Ng *et al* (2011) defines thermal inertia as "the property of a material that expresses the degree of slowness with which its temperature reaches that of the environment" and further encompasses the ability of an element to absorb and store heat. Concrete's high specific heat and low thermal conductivity yield a slow response to temperature change, resulting in a high thermal inertia compared to other building materials, such as steel. However, the thermal inertia of a concrete member can be altered by changing its cross section – more specifically the area of the cross section per unit width. By increasing the ratio of cross-sectional area per unit width of cross section, the thermal inertia of the section is also increased (Emerson 1976, Skorpen 2020). Therefore, sections with solid cores would have higher thermal inertia compared to voided sections with the same external dimensions. As a result, the temperature at the centre of a solid section should not show appreciable variation, while more sudden changes take place toward the exposed surface (Saetta *et al* 1995). Sections with higher thermal inertia will also have a smaller deformation response to changes in environmental temperature because the section itself absorbs or releases large amounts of heat before its mean temperature changes.

The temperature of concrete sections is an extensively researched topic, however, numerical and analytical models are most often calibrated or validated solely on comparisons between measured and predicted temperature distributions instead of measured strains. The purpose of this study was to both measure and model the thermal response of two concrete T-beams: one with a solid core and the other voided and therefore comparable to a box-girder, when subjected to environmental thermal loading. To achieve this, both T-beams were cast and instrumented with thermocouples and vibrating wire strain gauges, and the critical concrete material properties were tested. The measured strain in both sections was compared to the theoretically calculated strain values to validate the use of mathematical models and the associated assumptions. Additionally,

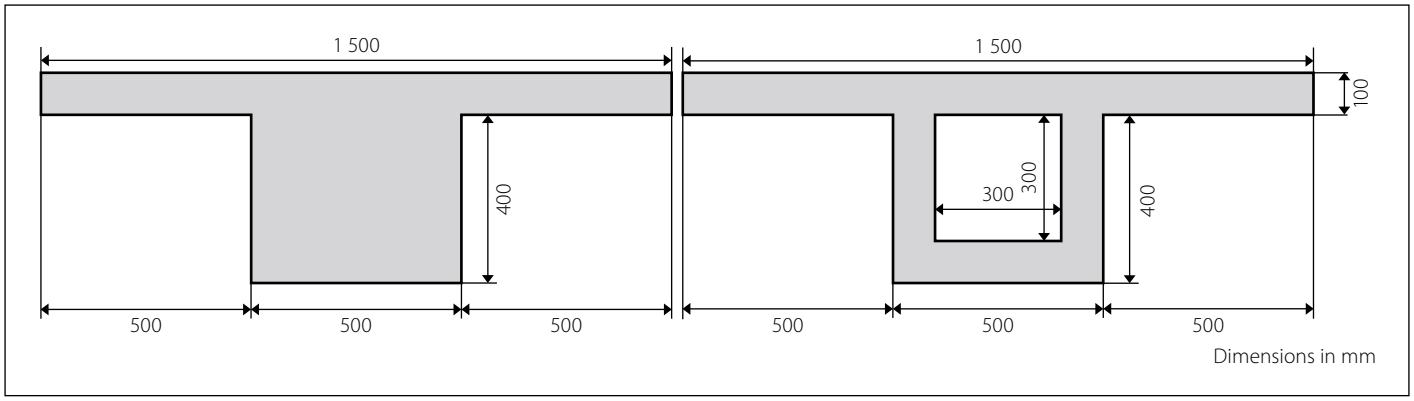

Figure 2 Cross-sectional dimension of the T-beams

self-equilibrating stresses were calculated for both sections. These stresses are important to consider as they develop from thermal curvature regardless of boundary condition.

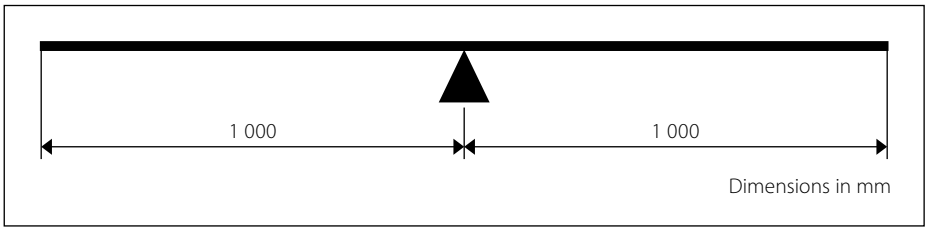

Figure 3 Cantilever arrangement

EXPERIMENTAL SETUP

Two concrete T-beams with different cross sections were cast for this study. The geometry of the solid T-beam was selected to be representative of the Van Zyl Spruit integral bridge constructed on the N1 between Trompsburg and Fonteintjie in South Africa (Skorpen 2020) and was reproduced at approximately half-scale for laboratory testing. A corresponding voided section with identical external dimensions was included to enable a direct comparative study, specifically to evaluate how reduced thermal inertia influences the thermal response. While the specimens were scaled for laboratory practicality, the reduced dimensions also allow the results to be relevant for smaller structural elements as well as larger bridge applications. The T-beams were cast and remained outside the Civil Engineering Laboratory of the University of Pretoria, situated in Hillcrest, Pretoria, South Africa. Instrumentation was embedded into the T-beams to measure temperature and strain caused by exposure to the outside environment. The beams were cast on an existing ground slab, strategically placed adjacent to one of the building's exterior walls. This location was chosen to provide convenient access to power for instrumentation while ensuring that the cables remained as protected as possible from potential interference. Furthermore, appropriate samples were cast and exposed to the same conditions as the beams to obtain representative concrete material properties.

T-beam configuration

The cross-sectional dimensions for the T-beams cast and analysed in this study are shown in Figure 2. The first section was a solid T-beam with a centre depth and width of 0.5 m and 1.5 m respectively. This cross section will be referred to as the 'solid' T-beam, beam, or section. The second T-beam had identical outer dimensions but with a 0.3 m square void in the centre portion of the beam, which will be referred to as the 'voided' T-beam, beam, or section. The thin sections on either side of the 0.5 m square segment will be referred to as flange sections for each beam.

Since strains can only be measured when the structure is free to move, the intention was to cast the beams in such a manner that they were unrestrained by external support as far as possible. If the unrestrained strains can be measured accurately, they can be fairly compared to theoretical calculated strains. As such, a cantilever setup was chosen, thereby avoiding support-related restraint as far as possible. Although this configuration was used for practicality in isolating free thermal strains, the observed thermal effects are not unique to cantilevers. By the principle of superposition, temperature-induced

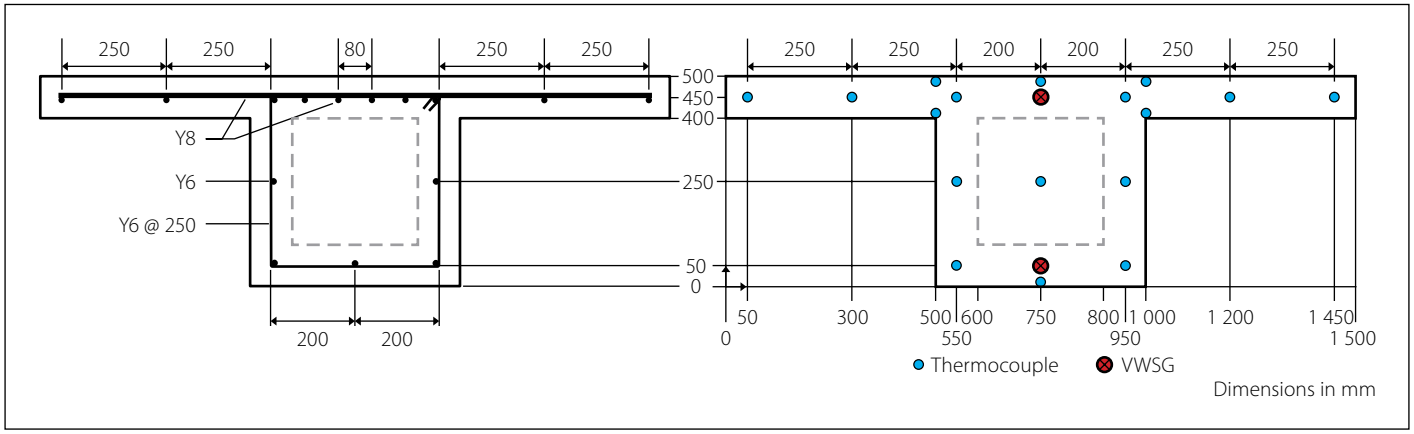

Figure 4 Reinforcement and instrumentation layout

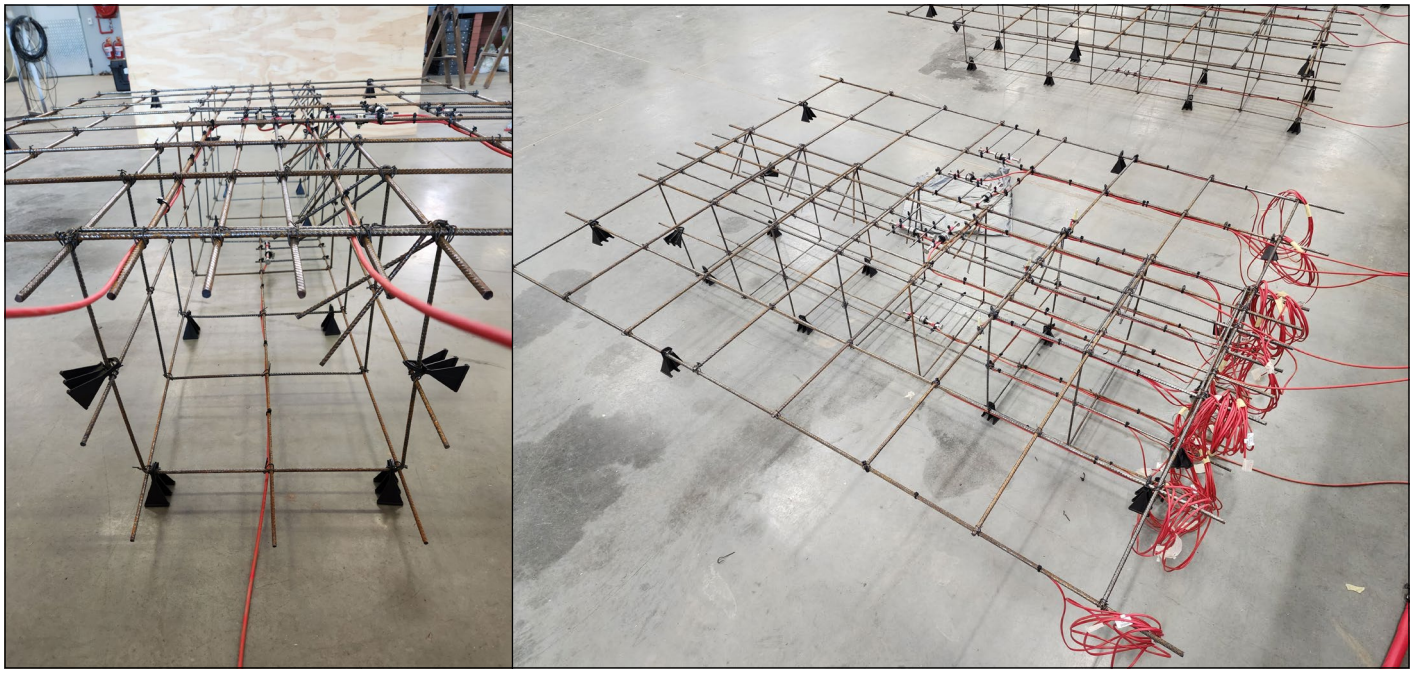

Figure 5 Instrumented reinforcement cages

strains and stresses interact with hogging and sagging moments depending on support conditions and temperature gradients, and are therefore relevant to continuous, simply supported and cantilever members alike. To ensure self-weight and creep strains were small enough to be considered negligible, the spans were kept small. The cantilever arrangement can be seen in Figure 3.

Reinforcement and instrumentation

The T-beams would be exposed to exclusively environmental loads, and because the T-beams cantilevered from the centre to either side, the reinforcement was calculated for a hogging bending moment. The required reinforcement was calculated according to Eurocode 2 for the self-weight of the solid T-beam, but minimum reinforcement governed the reinforcement requirements. The reinforcement layout, as shown in Figure 4, was used for both sections. Figure 4 also shows the positions of the thermocouples and vibrating wire strain gauges (VWSG) used to measure temperature and strain in the longitudinal direction, respectively.

Each VWSG contains an internal thermistor providing a means for temperature compensation as well as providing additional temperature measurements. The thermocouples' temperatures were calibrated against the VWSG thermistors to ensure the compatibility between the measurements obtained from the different instruments. This facilitated their concurrent use for the same calculations. The thermocouples were logged by Graphtec GL820 midi loggers and the VWSGs by a Campbell Scientific CR6 data logger. Both loggers captured data at 15 minute intervals for the duration of the study. Figure 5 shows one of the completed reinforcement cages with the instrumentation and related cabling fastened to the cage using zip ties.

Temperature distribution

Temperature measurements were used to produce vertical and transverse temperature distribution plots as well as calculated mean or effective temperatures for each of the cross sections. The vertical temperature distribution for the solid section was generated by using temperature points through the section's centre. For the voided section, the distribution was produced using temperatures through the web portion of the section. This was done throughout the study to accommodate the subsequent theoretical strain and stress calculations, as no strain nor stress can develop in the void of the section. Furthermore, to assist with strain and stress calculations, as well as to produce more detailed plots, additional temperature points were created through interpolation between measured points. Both measured and interpolated values are plotted for temperature figures and dependent strain and stress figures calculated from temperature.

Emerson (1976) refers to the mean temperature (T_m) described by Branco and Mendes (1993) as effective temperature (T_{eff}). T_{eff} is the weighted average temperature of the cross section and governs the longitudinal movement of a cross section. Equation 1 describes how the T_{eff} is calculated.

$$T_{eff} = \frac{\sum A_i \cdot T_i}{\sum A_i} \quad (1)$$

Where A_i is the area of the i^th discretised segment of the section and T_i the associated temperature of the same segment. The other temperature components described by Branco and Mendes (1993), δT and T_n are used implicitly in the calculation of calculated planar strain, curvature and self-equilibrating stress discussed in the next section.

Calculated strain and self-equilibrating stress caused by temperature

Theoretical strain caused by temperature is also derived from measured temperature through the cross section. The calculated strains were compared to the measured strains in the cross section and used in the calculation of self-equilibrating stress. These stresses arise from thermal curvature within the section and develop regardless of the external end conditions. The subsequent calculations were completed with the following assumptions:

- Plane sections remain plane during bending (Euler-Bernoulli beam theory holds)
- The beams remain uncracked and therefore effective stiffness remains constant
- Material properties are considered to be independent of temperature

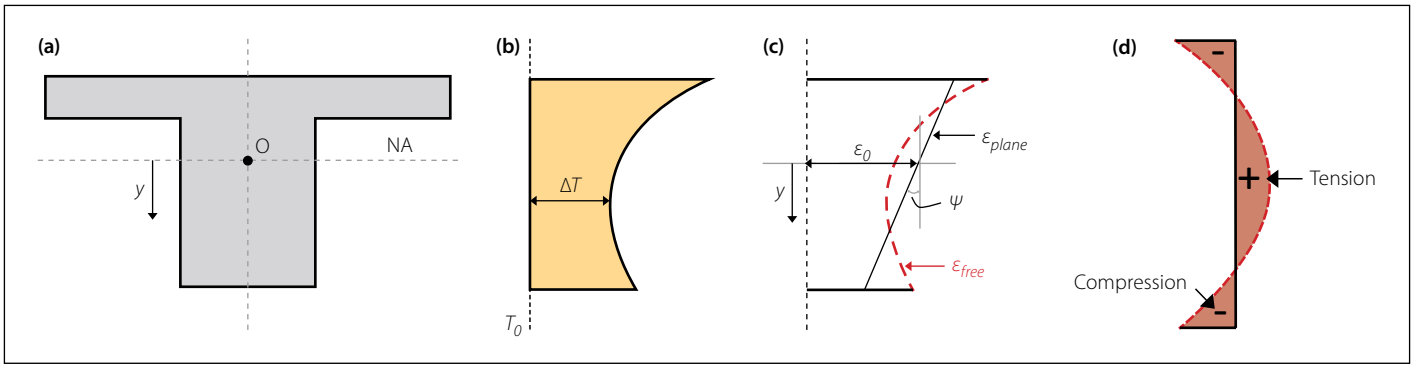

Figure 6 (a) Section, (b) vertical nonlinear temperature distribution, (c) strain profile, (d) self-equilibrating stress

- Thermal stress can be considered independent of stress and strain from other loading (principle of superposition is applicable).

Given that the calculated strains are integral to the computation of self-equilibrating stress, both aspects will be addressed together. The procedure is explained for a cross section with an arbitrary nonlinear temperature rise and with the methodology described by Priestly (1978), Ghali and Favre (1986), and Elbadry and Ghali (1986). The datum for the temperature change is represented by T_0. The datum is typically the temperature at a time where the temperature variation through the cross section is minimal. Figure 6 provides a visual representation of how the strains and self-equilibrating stresses were calculated.

For the cross section in Figure 6(a), the environmental temperature change induces a non-linear temperature rise, as shown in Figure 6(b), through the depth of the section. If each fibre in the beam was not restrained by the adjacent fibres and was free to expand, the hypothetical free strain would be of the same shape as the temperature distribution in Figure 6(b). The hypothetical free strain (ε_{free}) is indicated by the dashed line in Figure 6(c) and can be calculated at any coordinate using Equation 2 where α_c is the coefficient of thermal expansion of the concrete and $\Delta T_{(y)}$ is the change in temperature from the datum point to point y.

$$\varepsilon_{free} = \alpha \cdot \Delta T_{(y)} \quad (2)$$

If the strain is artificially prevented, the artificial stress required ($\sigma_{restraint}$) is given in Equation 3, where E is the modulus of elasticity of the material, assumed to be constant.

$$\sigma_{restraint} = -E \cdot \alpha \cdot \Delta T_{(y)} \quad (3)$$

The resultant artificial stress may be presented by an axial force (ΔN) and bending moment (ΔM) given in Equation 4 and Equation 5 respectively.

$$\Delta N = \int \sigma_{restraint} dA \quad (4)$$

$$\Delta M = \int \sigma_{restraint} y dA \quad (5)$$

The resulting axial strain (ε_0) at the centroid and curvature (ψ) are given by Equation 6 and Equation 7. A is the area of the cross section and is the second moment of area about the axis through the centroid.

$$\varepsilon_0 = -\frac{\Delta N}{EA} \quad (6)$$

$$\psi = \frac{\Delta M}{EI} \quad (7)$$

With the assumption that plane cross sections tend to remain plane and therefore produce linear strain profiles, the resulting plane strain (ε_{plane}) at any fibre is given by Equation 8. This plane strain was used to compare to the measured strain recorded by the VWSGs and validate the theoretical results.

$$\varepsilon_{plane} = \varepsilon_0 + \psi(y) \quad (8)$$

The resulting stress difference between the plane strain and the hypothetical free strain is called the self-equilibrating stress ($\sigma_{Self\text{-}eq}$), given by Equation 9.

$$\sigma_{Self\text{-}eq} = (-\varepsilon_{free} + \varepsilon_0 + \psi_{(y)}) \quad (9)$$

The self-equilibrating stress distribution is shown in Figure 6(d) and the sign convention for this study was as follows: positive stress indicates tension, and negative stress indicates compression relative to the plane stress plane produced by the plane strain.

Measured thermal strain

A VWSG measures frequency that is converted into strain by means of a gauge calibration factor. This initial strain needs to be temperature compensated for the gauge's coefficient of thermal expansion. Therefore, the total strain (ε_{total}) measured in the concrete at any point in time can be calculated with Equation 10 (RST Instruments 2019). The time of the initial readings coincides with the time at which T_0 is selected, and if the increment of strain analysed is small enough, the effects of concrete shrinkage are negligible. Furthermore, since the T-beams were only exposed to environmental thermal loads and the strain due to self-weight could be considered negligible, the total strain over a short period is equal to the thermal strain. This measured thermal strain was compared to the calculated plane strain to validate the mathematical model.

$$\varepsilon_{total} = (R_{n+1}^2 - R_n^2) \cdot CF + (T_{n+1} - T_n) \cdot \alpha_{gauge} \quad (10)$$

Where: R_n and R_{n+1} are the initial and subsequent frequency readings in $H_Z \times 10^{-3}$, respectively; CF is the gauge calibration factors provided by the manufacturer as 3.476; T_n and T_{n+1} are the initial and subsequent temperature readings in degrees Celsius, respectively, and α_{gauge} is the coefficient of thermal expansion of the gauge, equal to 12.2$\mu\varepsilon$/°C.

Mix design and material properties

Due to the scale of the T-beams, a concrete mixer truck was required to provide a large enough volume of concrete to cast the beams and material property samples in a single cast. A standard durability concrete mix (typical for bridge construction in South Africa) was ordered. The mix design proportions are given in Table 1.

After casting, the fresh concrete was covered with curing blankets until

Table 1 Concrete mix proportions

Material	Proportion	Unit [/m³]
High-strength cement (CEM I)	273.0	kg
Fly ash	77.0	kg
Quartzite stone (22 mm)	960.0	kg
Quartzite sand	707.0	kg
Washer filler sand	318.4	kg
Superplasticiser (Chryso Omega 180)	2.1	L
Water	180.2	L

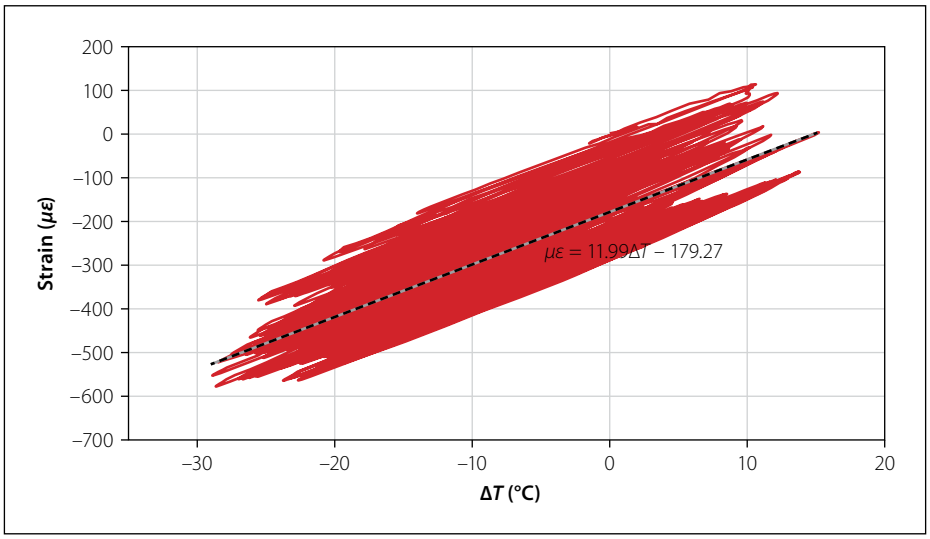

Figure 7 Strain versus ΔT for a 6-month period

Table 2 Representative material properties

Material property	Symbol	Value	Unit
Coefficient of thermal expansion of concrete	α_c	11.9	με/°C
28-day Concrete cube compressive strength	f_c	37	MPa
28-day Concrete split cylinder tensile strength	f_{ct}	3	MPa
28-day Concrete modulus of elasticity	E	26	GPa
Steel reinforcement modulus of elasticity	E_s	195	GPa

Table 3 Cross section properties

Cross section property	Solid	Voided
Cross sectional area [m²]	0.35	0.26
Neutral axis from soffit [mm]	308.5	328.5
Second moment of area (I) [mm⁴]	8.22×10^9	7.13×10^9
Area of cross section per unit width [m²/m]	0.233	0.173

the following day. The formwork and falsework supporting the flanges were removed three days after casting, while the ground supports at either end of the beams were removed one week after casting to create the cantilever shown in Figure 3. All instrumentation commenced recording before casting began and continued throughout the duration of the study.

The thermal response of any material is governed by its coefficient of thermal expansion (CTE), defined as the magnitude of strain that develops in response to a unit change in temperature. For this study, the CTE of the concrete was assumed to remain constant and was calculated using the same method as presented by Kada *et al* (2002), which uses the strain and temperature readings recorded by a vibrating wire extensometer to determine the CTE soon after set. The readings from a VWSG placed in the centre of a 0.125 m³ unreinforced cube, cast alongside the T-beams, were used in this study. The CTE of the concrete was calculated as 11.9 με/°C. Even though this value can vary over time due to moisture content variations, the assumed value of 11.9 με/°C remains a good estimate, as can be seen by the correlation to the average slope plotted in Figure 7 over a period of 6 months.

The tested representative material properties for the concrete and reinforcement are presented in Table 2. The 28-day compressive strength was determined on 100 mm cube specimens in accordance with SANS 5863:2006, while the tensile splitting strength was determined on 100 mm diameter cylinders in accordance with SANS 6253:2006. The static modulus of elasticity of the concrete was determined using 100 mm diameter cylinders based on ASTM C469:2014, and the modulus of elasticity of the reinforcing steel was determined by tensile testing consistent with SANS 6892-1:2010.

Figure 8 T-beam cross sections

Completed T-beams and associated cross-sectional properties

The cross-sectional properties for both T-beams are presented in Table 3. Figure 8 and Figure 9 display the T-beams' cross sections and the cantilever configuration used for the study. The beams were cast on the north side of a north-facing wall, leaving them fully exposed to solar radiation throughout the day; the effect of building shadowing can therefore be disregarded. As the beams were situated outdoors, they were also exposed to other natural elements such as wind and rainfall. Although their proximity to the ground slab meant that heat radiation from the slab could influence the temperature readings, both beams were placed directly adjacent to one another and therefore experienced identical boundary conditions. This ensures that any comparative evaluation between the two cross sections is not biased by differences in exposure. It should also be noted that in Figure 8 the voided section appears open at one end because the polystyrene infill was temporarily removed for the purpose of the photograph. During the study, the polystyrene remained in place at both ends, so the void was closed, more closely resembling the interior of a box girder section.

Figure 9 T-beam cross section – cantilever

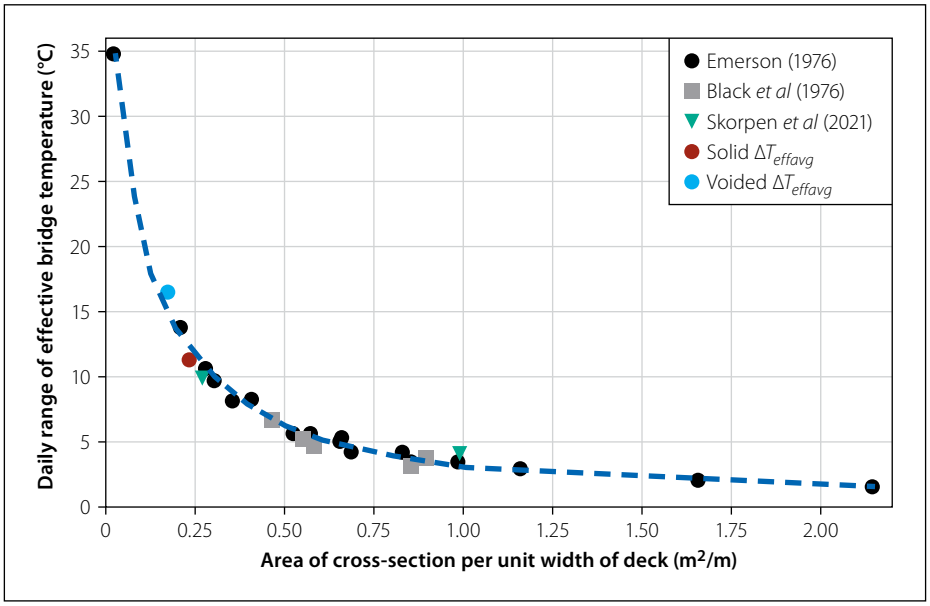

Figure 10 Daily effective temperature range versus area of cross section per unit deck width

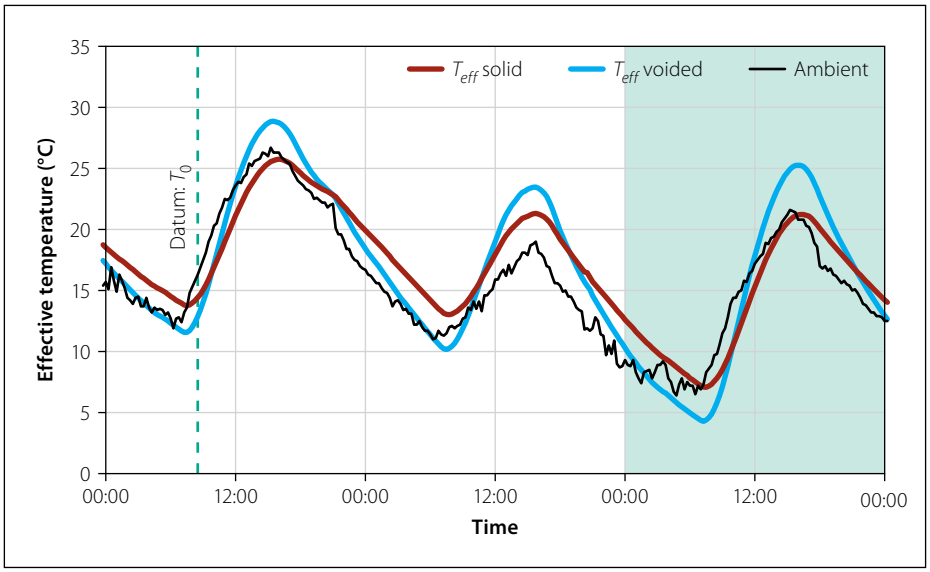

Figure 11 Effective temperatures for a representative three-day period

RESULTS

Black *et al* (1976) showed that daily effective temperature can be related to the thermal inertia of a cross section, more specifically the area of the cross section per unit width of a bridge deck. Emerson (1976) expanded on these results by calculating the daily temperature range of sixteen different cross sections for a day with high solar radiation and a large range of shade temperature to produced large effective temperature ranges. In this study, the measured average and daily temperature ranges for the solid and voided T-beams over a 6-month period were 11.4°C and 16.7°C respectively. These values were plotted against the area of the cross section per unit width, alongside the results presented by Black *et al* (1976), Emerson (1976) and Skorpen *et al* (2021) in Figure 10.

The results from the present study showed good correlation to the trend observed by the mentioned authors and highlights the relationship between thermal inertia and thermal response. It should be noted that although only two half-scale specimens were tested, their inclusion extends the available dataset in the range where relatively few experimental results exist. The smaller scale of the specimens demonstrates that the observed trend is not restricted to large bridge decks but is also applicable to smaller structural members. For this study, an increase of cross-sectional area per unit width of 34% reduced the range of effective temperature by 31%. The reduction in effective temperature is directly related to the longitudinal movement of the member and, as such, it is clear that less expansion and contraction is expected by a solid section when compared to a box girder. This can be particularly advantageous when smaller thermal movements are required.

Analysis of a typical day

As mentioned previously, the temperature distributions through the cross sections are

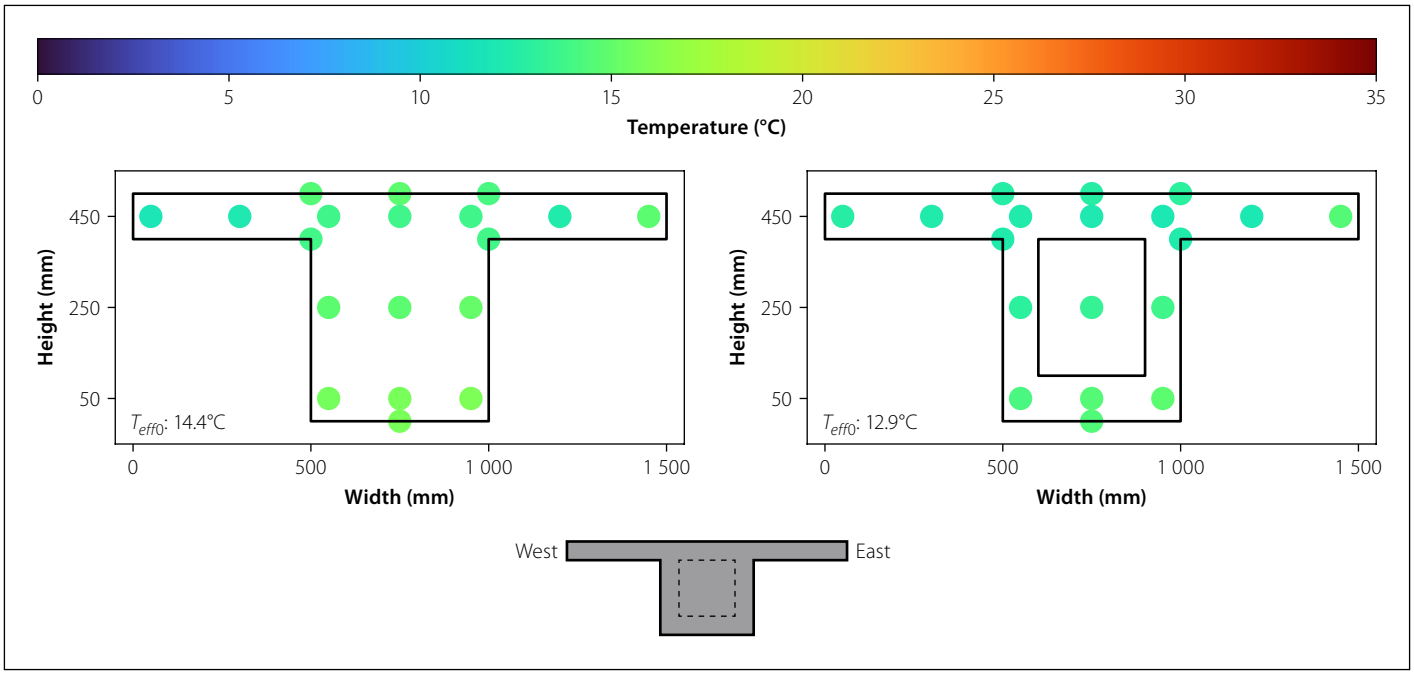

Figure 12 Temperature distributions at the selected datum for a representative three-day period

required to calculate the strain and stress distributions of the T-beams. The complete temperature distribution throughout the cross section of both solid and voided T-beams is given for a typical day, after which the vertical and transverse temperature distributions for the same day are isolated and presented.

To ensure a fair comparison between the cross sections, a representative three-day period was selected six months after casting, during which no rainfall or extreme temperature events occurred. The effective temperatures for both cross sections and the ambient shade temperature for the selected period are presented in Figure 11. The figure reiterates the daily difference between the cross sections and demonstrates a good correlation between ambient shade temperature and effective temperature.

To complete the subsequent calculations, a datum temperature was selected at a time where the effective temperatures were similar for both T-beams and the temperature distributions throughout the cross sections were as uniform as possible. The selected datum (T_0) is denoted by the green dashed line in Figure 11 and the temperature distributions for both T-beams are illustrated in Figure 12. The chosen datum allowed fair comparison of the different cross sections in both vertical and transverse directions. The effective temperatures for each cross section at the selected datum are given as T_{eff0} in Figure 12.

The 24-hour period shaded in green in Figure 11 was selected as the day to compare the temperature distributions and behaviour of the different cross sections, since it contained the largest range in ambient temperature of the three days. Figure 13 and Figure 14 contain the full temperature distributions for both cross sections at intervals of three hours for the selected day. The orientation of the beams was the same as in Figure 12, where the flange denoted by the width measurement of 0 mm pointed toward the west, and the flange denoted by the 1500 mm pointed toward the east. As in Figure 12, the effective temperatures at the selected datum are given at the bottom left as T_{eff0} for each time in Figure 13 and Figure 14. Similarly, the effective temperature for each time and cross section are given at the bottom right as T_{eff}.

At 00:00 on the selected day, both T-beams still retained some of the heat from the day before at their cores. The solid beam's core had a higher temperature than the voided beam, which contributed to the higher effective temperature for the time as well, however the flange temperatures were similar. The cores and flanges continued to cool down as the retained heat from both T-beams continued to dissipate. The lowest effective temperatures were reached at 06:00 and 07:00 for both beams. The core of the solid T-beam remained warmer than the voided T-beam's core, while the edges of both beams' flanges dropped to below 5°C. As the sun rose, the east-facing flanges gained heat first, and as the time progressed to midday the top portions gradually displayed even temperatures. The maximum effective temperatures were reached shortly after 15:00, and while both T-beams' flanges showed temperatures of approximately 30°C, the top centre part of the solid T-beam remained markedly cooler, while the top centre part of the voided T-beam reached similar temperatures to the flanges. As the sun descended, the west-facing flanges retained their heat while the east-facing flanges began to cool down. Notably the effective temperatures at 21:00 were very similar for the two T-beams, but the voided section's temperature was quicker to respond to environmental conditions, which was expected due to its lower thermal inertia.

The vertical temperature distributions for the selected day were isolated and plotted at three-hour intervals to generate Figure 15. Based on this plot, the difference in mean temperature and temperature range between the T-beams is once again evident. Additionally, the difference between top and bottom temperature for both beams is more clearly defined. The vertical temperature distribution shapes for both cross sections match the nonlinear temperature profiles presented in literature of experimental work (Peirettie *et al* 2014, Gu *et al* 2014).

The presence of the void had a significant effect on the shape of the temperature distribution through the depth of the beam, creating a more prominent 'C-' or mirror 'C-' like shape at the warmest time, compared to the solid beam. Despite the higher temperature at the top of the beam at the warmest time of the day, and the greater mean temperature of the voided beam, the gradients between the beams remain similar. This is confirmed by the similar trend in calculated thermal

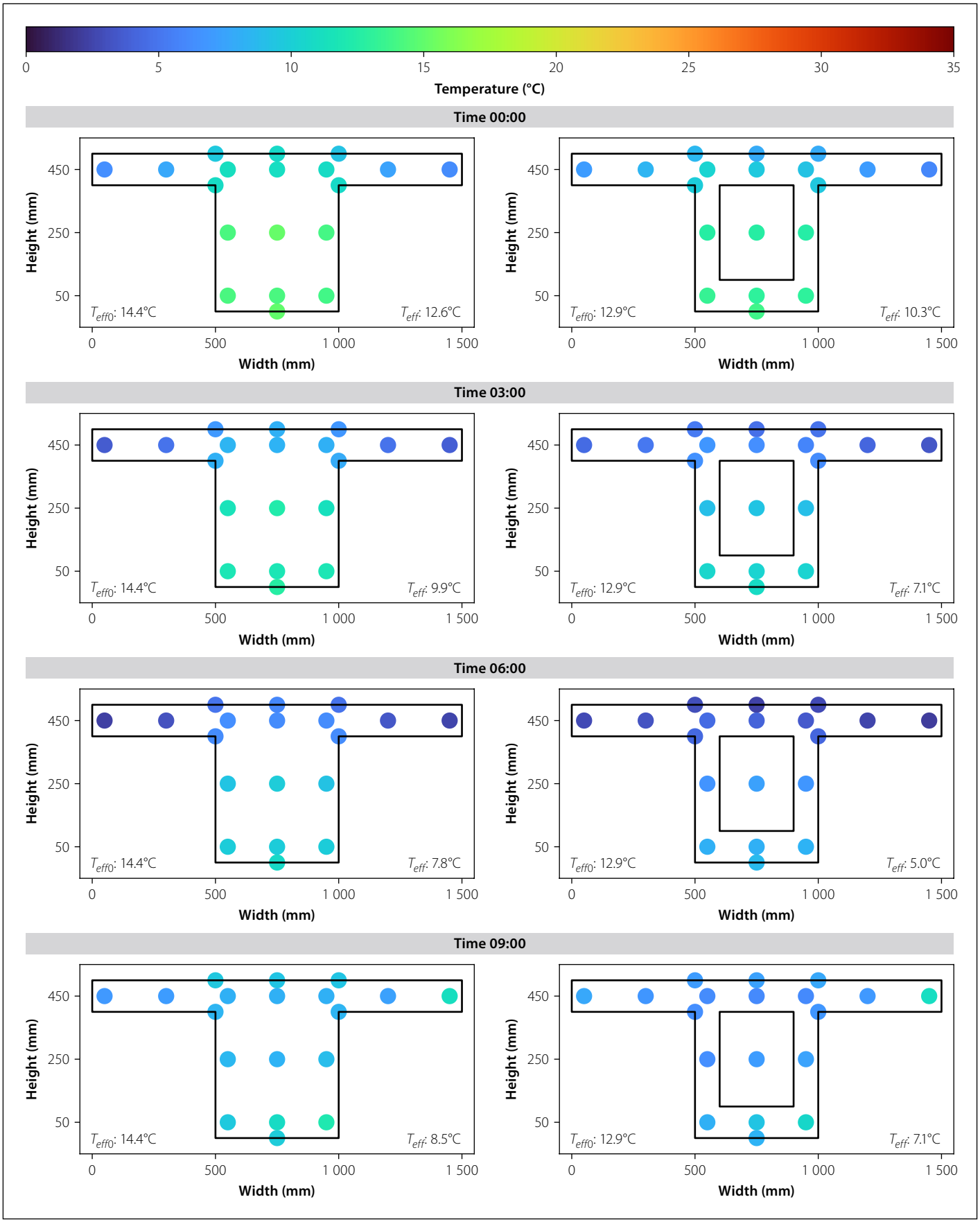

Figure 13 Temperature distributions from 00:00 to 09:00

bending moments for the three-day period given in Figure 16. The figure also emphasises the significant moments that are produced in both sections solely due to thermal loading caused by the environment. Since some authors highlighted the importance of transverse temperature distributions, the transverse temperatures were plotted for the same time intervals in Figure 17. The transverse temperatures of the voided beam were fairly uniform for the flanges and centre portion, which can be explained by the uniform thickness across the top portion of the beam because of the void.

The temperatures in the flanges of the solid beam were similar to the voided beam's flanges, but contrastingly, the solid beam's centre segment lagged behind the

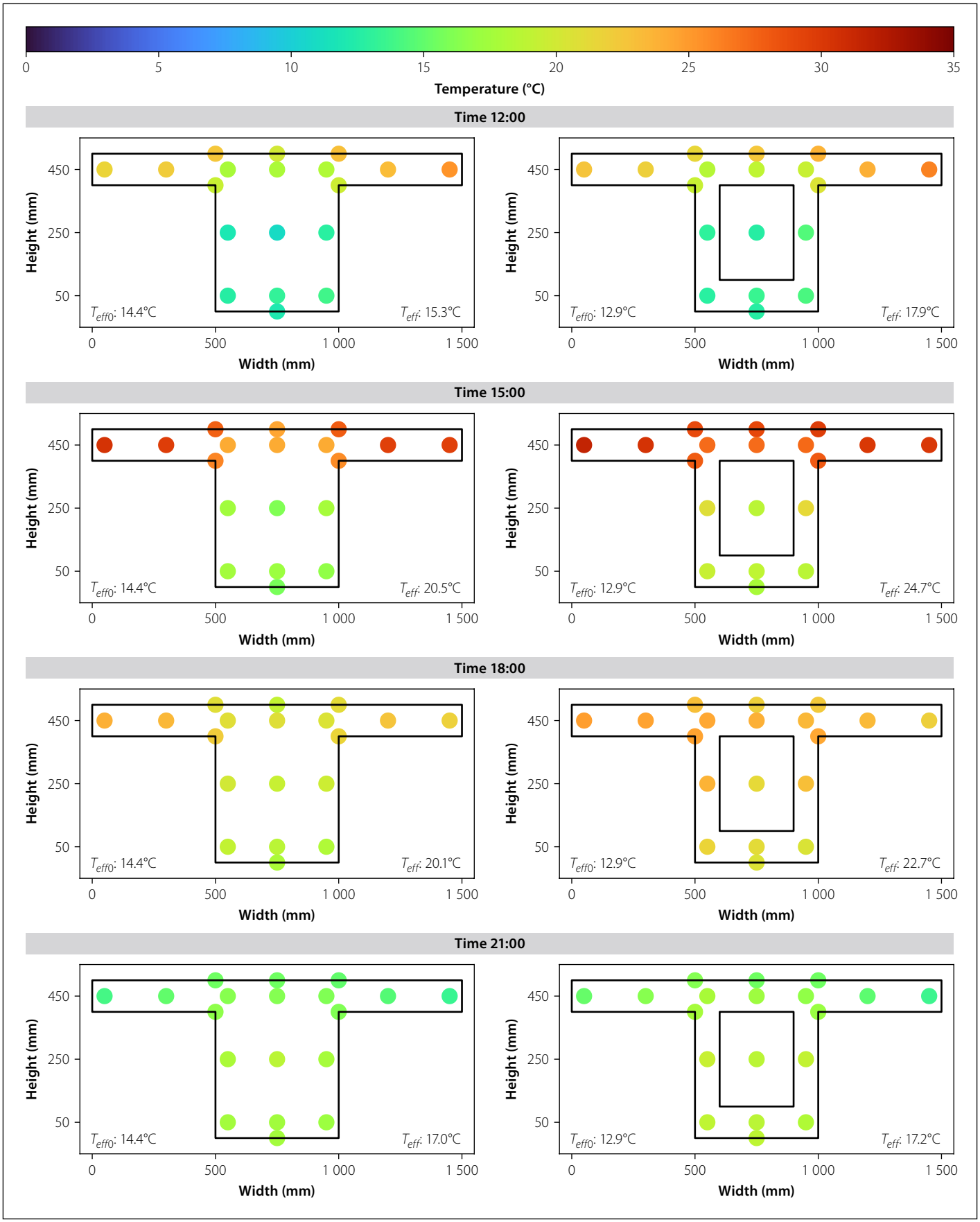

Figure 14 Temperature distributions from 12:00 to 21:00

temperature in the flanges, causing large temperature differentials between the two parts. The large temperature difference will create a difference in longitudinal and transverse movements between the two segments, which in turn causes large stresses at the intersection between the web and flange regions. This highlights the need to consider the transverse temperature distributions especially when a large difference in thickness is present between the top slab and the web beneath it. To reduce the temperature difference the flange to web thickness ratio should be optimised and the utilisation of chamfering should be considered.

It follows from the temperatures presented before that the temperature distributions

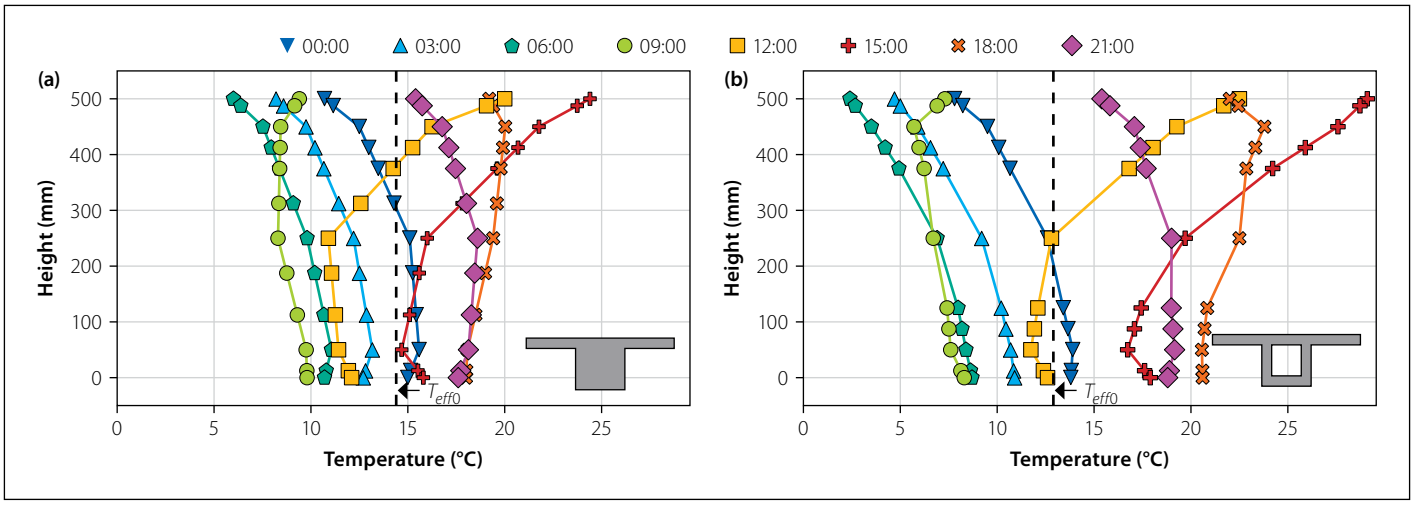

Figure 15 Daily vertical temperature distributions for the (a) solid and (b) voided T-beams on the selected day

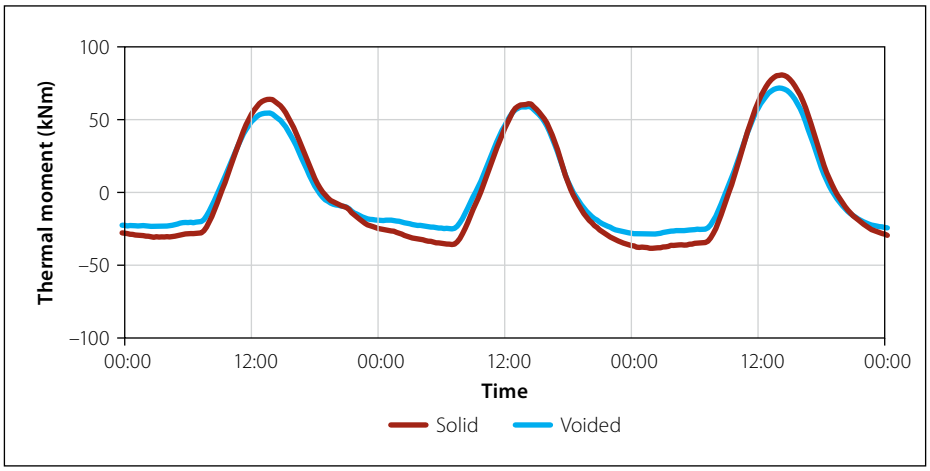

Figure 16 Thermal moments induced by restraint of curvature

in both sections were non-linear in both the vertical and transverse directions. Hence, self-equilibrating stresses would develop. In order to calculate these stresses, the hypothetical free strain and theoretical plane strain caused by temperature were calculated and analysed. Figure 18 presents the plane strains produced through the application of Euler-Bernoulli beam theory as the shaded T-shapes and the hypothetical free strains are indicated by dashed lines, for two critical time increments of the solid T-beam. The same principles apply to the voided beam, but the solid beam is used in the interest of visual clarity. This illustration emphasises the difference in strain between the top and bottom of the beam, creating curvature and thermal bending moments when restrained. Additionally, the difference between the plane and hypothetical strains in both the vertical and transverse directions are clearly visible. This allows the incompatibility condition which gives rise to self-equilibrating stresses to be seen.

The self-equilibrating stresses are plotted in the vertical and transverse directions in Figure 19. Tensile stresses are indicated by positive values and conversely, compressive

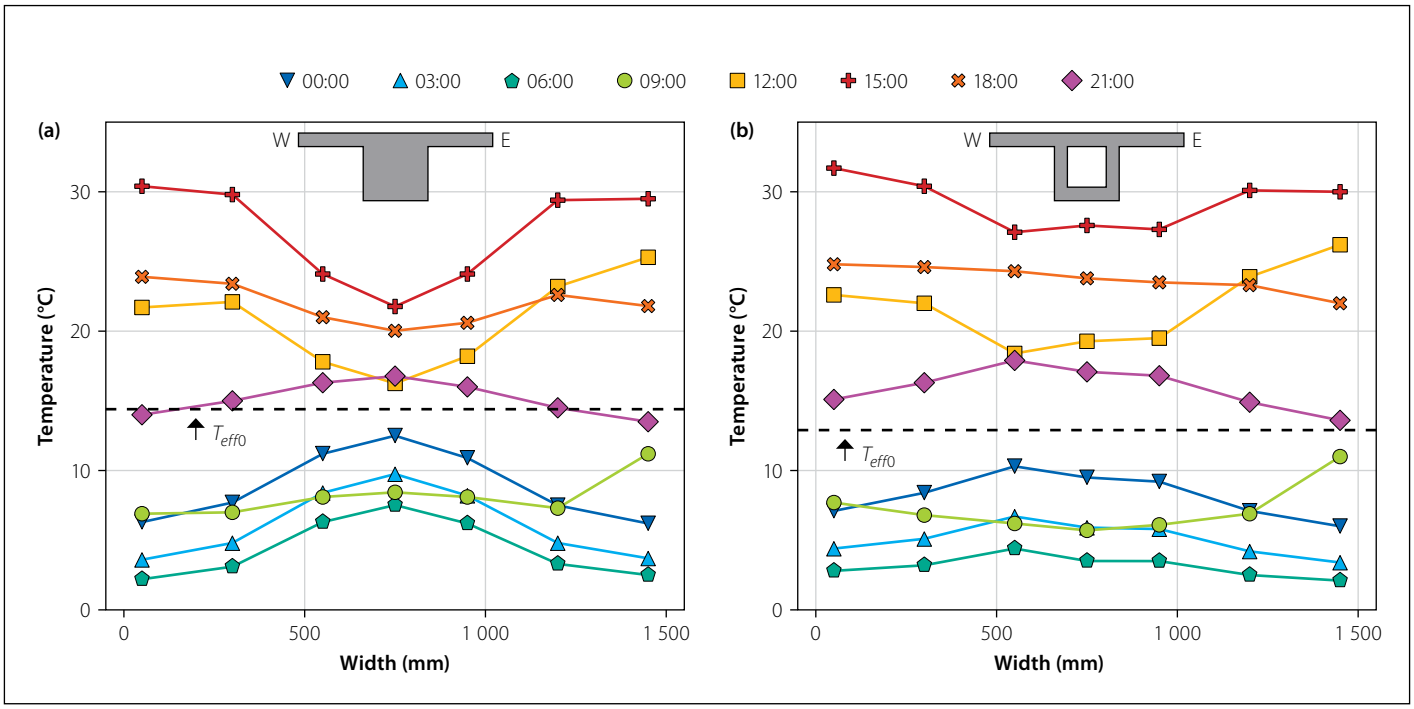

Figure 17 Daily transverse temperature distributions of the (a) solid and (b) voided T-beams on the selected day

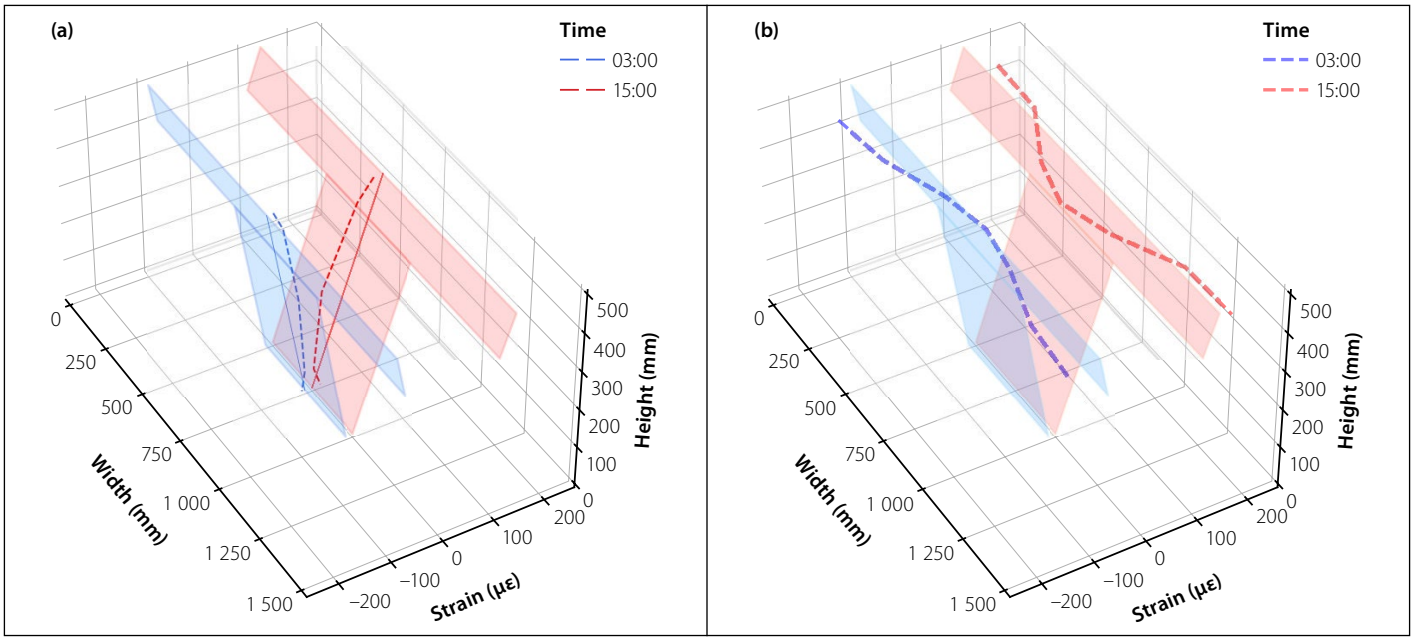

Figure 18 Hypothetical free (a) vertical and (b) transverse strains and strain planes

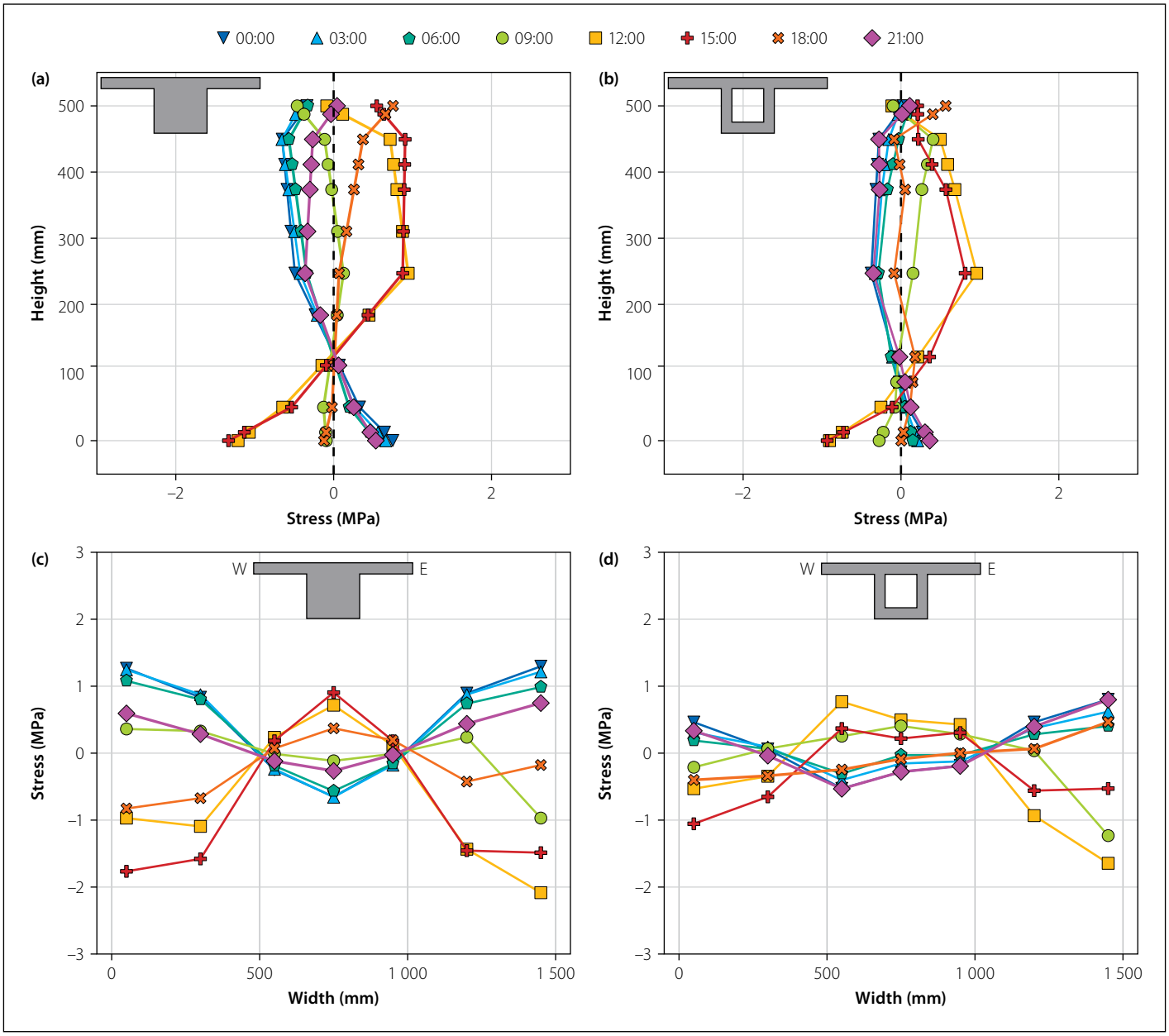

Figure 19 Vertical self-equilibrating stress for the (a) solid and (b) voided T-beams and transverse self-equilibrating stress for the (c) solid and (d) voided T-beams

stresses by negative values. In the vertical direction, the two profiles produce similar shapes, with near identical stresses at the centre of the sections. However, the solid section produced larger stresses at the top and bottom surfaces compared to the voided section. The vertical self-equilibrating stresses of box girder sections, similar to the voided T-beam in this study, were the main focus throughout literature.

The shape of the self-equilibrating stress profiles in this study is similar to those reported by Elbadry and Ghali (1986). Elbadry and Ghali (1986) however had a much larger section 2.74 m deep and recorded self-equilibrating tensile stresses of approximately 2.5 MPa in the beam's centre, which suggests deeper sections may develop greater self-equilibrating stresses. Both cross sections' self-equilibrating stresses remained below the tensile strength of the concrete measured at just over 3 MPa at the time under consideration. Therefore, the vertical self-equilibrating stresses should not result in the formation of cracks within either of these sections.

In the transverse direction, the self-equilibrating stresses also remained below the concrete tensile strength and the largest stresses observed were compressive stresses in the flanges of the solid section. Even though the largest stresses were compressive, there was a significant difference in stress between the centre and the flanges of the solid beam for the warmest and coldest times of the day. Contrastingly, the stresses in the transverse direction were more uniform across the width of the voided section. Although the tensile strength of the concrete is not exceeded by the self-equilibrating stresses, these stresses should be considered within calculations since they equate to approximately 30% of the concrete's ultimate tensile capacity.

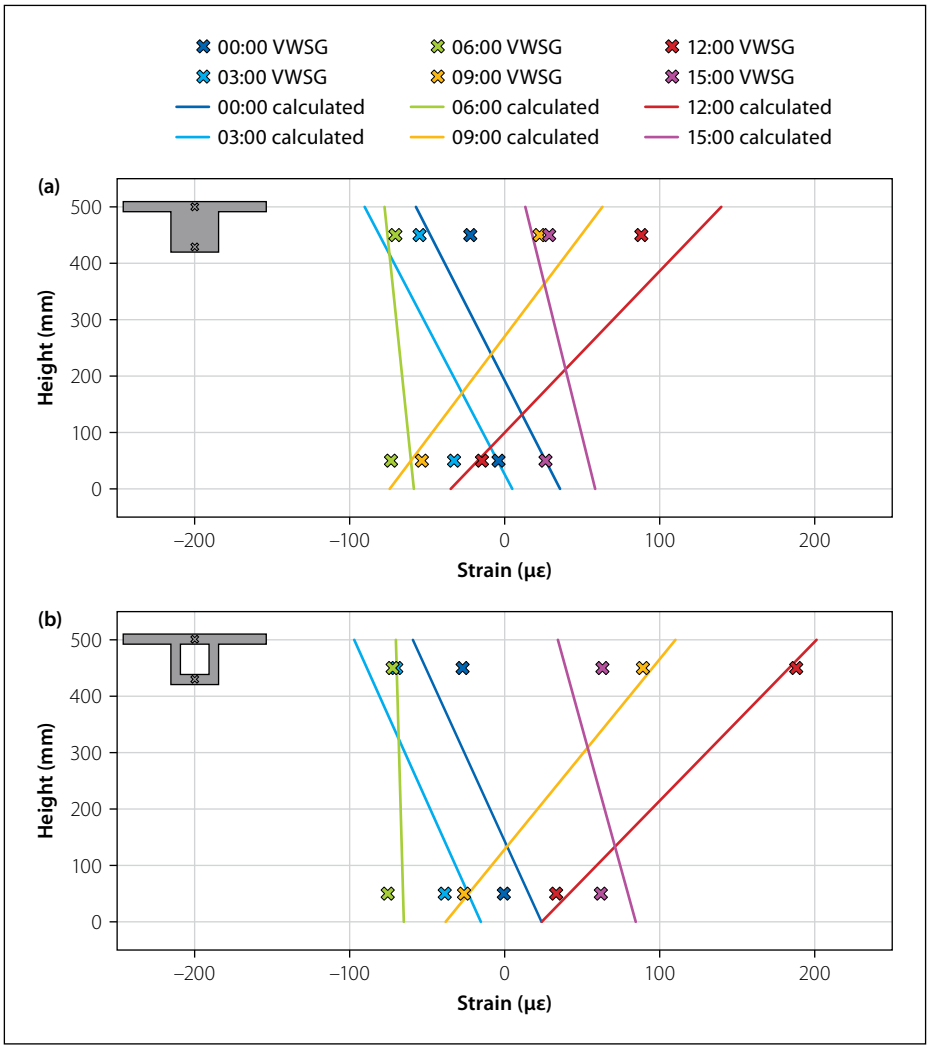

Figure 20 Measured and calculated strains for the (a) solid and (b) voided T-beams

COMPARISON BETWEEN CALCULATED AND MEASURED STRAINS

In the previous calculations, the stresses and strains were derived by means of mathematical modelling using the actual temperature measurements as the basis. There was therefore a need to assess the validity of the results. To achieve this, the strains recorded by the VWSGs in each T-beam were compared to the calculated strains for the same selected day and datum time. The strains were zeroed at the datum time to exclude any prior shrinkage history, ensuring that only the thermal effects of the selected day were compared. Since the comparison is referenced to the same datum and the analysed time window is short, the effects of shrinkage and creep during this period can be regarded as negligible.

The comparison between the measured and calculated strains are given in Figure 20. The calculated strains are presented as a straight line representing the strain plane (ε_{plane}), while the single measurement points are indicated by cross markers at positions where the VWSGs were embedded into the concrete. For the voided T-beam, the calculated strains matched the measured values for the included warmest (15:00) and coldest (06:00) times well, even though some variation occurred between these times. Since the calculated strains at these critical times matched the measured strains well, the mathematical model is considered representative and valid. In the case of the solid beam, the strains calculated for coldest time (06:00) matched the measured strains well but overestimated the curvature at other times. In this case the mathematical model produces conservative estimations of reality.

The difference between measured and calculated strains can be explained by the presence of cracking caused by the high stresses induced between the flange and web segments of the solid section as a result of the large temperature differences which develop between the two regions. A critical assumption that forms part of the mathematical model is that the sections remain uncracked. With the presence of cracks, the contribution of the flanges toward the section behaviour is altered because the section properties are adjusted. The influence of the flanges on the moment and curvature could have been reduced by cracking within the T-beam, thereby causing the overestimation of the calculated strains.

CONCLUSION

This study included both experimental and theoretical results for the influence of environmental thermal loading on two concrete T-beams with different cross-sectional geometry. The key findings are summarised as follows:

- The mathematical models provided acceptable predictions of the strains

developed due to thermal loads. Cracking caused by high stresses induced between the flange and web resulted in differences between the calculated and measured thermal strains.

- The most prominent difference between the two sections is the effective temperature and associated longitudinal strain. The higher thermal inertia of the solid section reduced the effective temperature of the cross section. This resulted in smaller longitudinal movements occurring and, in the presence of restraint, would cause smaller stresses when compared to the voided section. As such, solid sections can be advantageous when thermal movement or stresses needs to be minimised or reduced for applications such as integral bridge construction.
- Significant bending moments can develop within beams due to thermal environmental loading when curvature is prevented, regardless of cross section.
- Transverse temperature distributions should be considered when large thickness differences between the slab and web are present in solid sections. The utilisation of chamfering can reduce large, localised temperature differences across the width of the section. Uniform thickness also aids in reducing temperature differentials in the transverse direction.
- In this study, the self-equilibrating stresses that developed within both cross sections were not large enough to exceed the tensile strength of the concrete and cause cracking. However, these stresses should be considered in conjunction with the stresses induced due to the relevant boundary conditions and expected live loads.

DATA AVAILABILITY STATEMENT

Some or all data, models, or code that support the findings of this study are available from the authors upon reasonable request.

ACKNOWLEDGEMENTS

The South African National Roads Agency (SANRAL) is gratefully acknowledged for supporting this study, which formed part of the broader SANRAL research project on integral bridges, contract number: 1002-58600-2018 P7a2. AfriSam is appreciatively recognised for providing the readymix concrete used to cast the T-beams instrumented and analysed in this study.

REFERENCES

Abid, S R. 2018. Three-dimensional finite element temperature gradient analysis in concrete bridge girders subjected to environmental thermal loads. *Cogent Engineering*, 5(1): 1447223.

Abid, S R, Tayşi, N, Özakça, M, Xue, J & Briseghella, B. 2021. Finite element thermo-mechanical analysis of concrete box-girders. *Structures*, 33: 2424–2444.

ASTM International. 2014. *ASTM C469/C469M-22: Standard test method for static modulus of elasticity and Poisson's ratio of concrete in compression.* West Conshohocken: ASTM International.

Black, W, Moss, D S & Emerson, M. 1976. *Bridge temperatures derived from measurement of movement*, TRRL Report LR 748. Wokingham: Department of the Environment (Transport and Road Research Laboratory).

Branco, F A & Mendes, P A. 1993. Thermal actions for concrete bridge design. *Journal of Structural Engineering*, 119(8): 2313–2331.

Dilger, W H, Ghali, A, Chan, M Y T, Cheung, M S & Maes, M A. 1983. Temperature stresses in composite box girder bridges. *Journal of Structural Engineering*, 109(6): 1460–1478.

Elbadry, M & Ghali, A. 1986. Thermal stresses and cracking of concrete bridges. *ACI Journal*, 83(6): 1001–1009.

Emerson, M. 1976. *Extreme values of bridge temperatures for design purposes*, TRRL Report No. 744. Crowthorne: Transport and Road Research Laboratory.

Feng, Z, Jinyi, L & Lei, G. 2022. Experimental investigation of temperature gradients in a three-cell concrete box-girder. *Construction and Building Materials*, 335: 127413.

Fu, H, Ng, S T & Cheung, M S. 1990. Thermal behavior of composite bridges. *Journal of Structural Engineering*, 116(12): 3302–3309.

Ghali, A & Favre, R. 1986. *Concrete Structures: Stresses and Deformations.* London: Chapman & Hall.

Gu, B, Chen, Z & Chen, X. 2014. Temperature gradients in concrete box girder bridge under effect of cold wave. *Journal of Central South University*, 21(3): 1227–1241.

Hagedorn, R, Martí-Vargas, J R, Dang, C N, Hale, W M & Floyd, R W. 2019. Temperature gradients in bridge concrete I-girders under heat wave. *Journal of Bridge Engineering*, 24(8).

Hoffman, P, McClure, R M & West, H. 1983. Temperature study of an experimental segmental concrete bridge. *PCI Journal*, 28(2): 78–97.

Imbsen, R A, Vandershaf, D E, Schamber, R A & Nutt, R V. 1985. *Thermal effects in concrete bridge superstructure*, NCHRP Report 276. Washington, DC: Transportation Research Board, National Research Council.

Kada, H, Lachemi, M, Petrov, N, Bonneau, O & Aïtcin, P C. 2002. Determination of the coefficient of thermal expansion of high performance concrete from initial setting. *Materials and Structures*, 35(1): 35–41.

Lee, J H. 2012. Investigation of extreme environmental conditions and design thermal gradients during construction for prestressed concrete bridge girders. *Journal of Bridge Engineering*, 17(5): 547–556.

Mirambell, E & Aguado, A. 1990. Temperature and stress distributions in concrete box girder bridges. *Journal of Structural Engineering*, 116(9): 2388–2409.

Moorty, S & Roeder, C W. 1992. Temperature-dependent bridge movements. *Journal of Structural Engineering*, 118(4): 1090–1105.

Moravcik, M & Krkoska, L. 2017. Thermal effects on box girder concrete bridges. *Key Engineering Materials*, 738: 273–283.

Ng, S C, Low, K S & Tioh, N H. 2011. Newspaper sandwiched aerated lightweight concrete wall panels: Thermal inertia, transient thermal behavior and surface temperature prediction. *Energy and Buildings*, 43(7): 1636–1645.

Peiretti, H C, Parrotta, J E, Berecibar Oregui, A, Perez Caldentey, A & Ariñez Fernandez, F. 2014. Experimental study of thermal actions on a solid slab concrete deck bridge and comparison with Eurocode 1. *Journal of Bridge Engineering*, 19(10).

Potgieter, I C. 1983. *Response of highway bridges to nonlinear temperature distributions.* PhD thesis. University of Illinois Urbana-Champaign.

Priestley, M J N. 1972. Model study of a prestressed concrete box-girder bridge under thermal loading. *Proceedings*, 9th AIBSE Congress: 737–746.

Priestley, M J N. 1978. Design of concrete bridges for temperature gradients. *Journal of the American Concrete Institute*, 75(5), 209–217.

Radolli, M & Green, R. 1975. Thermal stresses in concrete bridge superstructures under summer conditions. *Transportation Research Record*, 547: 23–36.

Roeder, C W. 2003. Proposed design method for thermal bridge movements. *Journal of Bridge Engineering*, 8(1): 12–19.

RST Instruments Ltd. 2019. *Vibrating Wire Embedment Strain Gauge (VWSG-E) Manual*, Document No. ELM0085C, Rev. C. Maple Ridge: RST Instruments Ltd.

Saetta, A, Scotta, R & Vitaliani, R. 1995. Stress analysis of concrete structures subjected to variable thermal loads. *Journal of Structural Engineering*, 121(3): 446–457.

Skorpen, S A. 2020. *Temperature effects and the behaviour of long reinforced concrete integral bridges.* PhD thesis. University of Pretoria.

Skorpen, S A, Kearsley, E P, Clayton, C R I & Kruger, E J. 2021. Structural monitoring of an integral bridge in South Africa. *Smart Infrastructure and Construction*, 173(2): 63–73.

Vecchio, F J. 1987. Nonlinear analysis of reinforced concrete frames subjected to thermal and mechanical loads. *ACI Structural Journal*, 84(6): 511–521.